Surrogate based optimisation of a pump mode startup sequence for a contra-rotating pump-turbine using a genetic algorithm and computational

Journal of Energy Storage 62 (2023) 106902

Contents lists available at ScienceDirect

Journal of Energy Storage

journal homepage: www.elsevier.com/locate/est

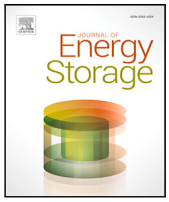

Research paper

Surrogate based optimisation of a pump mode startup sequence for a contra-rotating pump-turbine using a genetic algorithm and computational fluid dynamics

Jonathan Fahlbeck *, Håkan Nilsson, Saeed Salehi

Division of Fluid Dynamics, Department of Mechanics and Maritime Sciences, Chalmers University of Technology, Gothenburg SE-412 96, Sweden

ARTICLE INFO

Keywords:
Pumped hydro storage
Startup operation
Surrogate based optimisation
Gaussian-process
Computational fluid dynamics
Optimising transient

ABSTRACT

Contra-rotating pump-turbines (CRPT) have been proposed as a new solution for pumped hydro storage (PHS) at low-head sites. The two individually operated runners give both flexibility and complexity during transient operation, such as startup. This paper presents an optimisation approach for the pump mode startup sequence of a CRPT. The aim is to minimise the loads during fast startups and thus extend the lifetime and increase the flexibility of the CRPT. The startup sequence is decomposed into five design variables which determine a valve opening and the speedup of each runner rotational speed. The optimisation procedure includes transient computational fluid dynamics (CFD) simulations and global surrogate-based optimisation (SBO). An objective function, based on an integration of the time derivative of the axial force, is derived and transformed into a Gaussian-process surrogate model. The results show that the SBO can predict an optimal combination of the five variables that limits unfavourable load variations during the pump mode startup sequence. For an optimal startup sequence, the valve should be opened up during 73% of the sequence, the upstream runner should speed up during most of the sequence, and the downstream runner should speed up during the final third of the sequence. The outcome of this work is beneficial for a safe startup operation of possible future PHS with CRPTs.

1. Introduction

The most common form of energy storage provided today is through pumped hydro storage (PHS) [1]. The historical development of PHS has mainly focused on high-head applications of several hundreds of meters. The large difference in height elevations between the reservoirs for high-head PHS limits where it can be built [2,3]. To overcome this and to allow energy storage at low-head locations with flat topography, new pump-turbine designs are needed. The ALPHEUS (augmenting grid stability through low head pumped hydro energy utilization and storage) Horizon 2020 EU [4,5] project is an attempt to address low-head pump-turbine designs. One of the concepts investigated in the ALPHEUS project is an axial flow, shaft-driven, reversible contra-rotating pump-turbine (CRPT).

A CRPT has two individual runners, rotating in opposite directions from one another. This type of runner, or propeller, configuration is traditionally associated with maritime and aviation propulsion systems [6], but it has recently been proposed as an alternative runner configuration for low-head PHS [2,7]. Several researchers have performed experimental and numerical studies of CRPTs, indicating its potential as a low-head runner configuration [8–13]. Kim et al. [8] demonstrated that the $k-\omega$ shear stress transport (SST) turbulence model gives a good accuracy for steady-state operations of a small CRPT. Later, the same research group performed a design and optimisation study reaching hydraulic efficiencies of up to 79.98% and 86.23% in pump and turbine modes, respectively, for the optimal design [9]. Vagnoni et al. [10] presented numerical and experimental results of a contra-rotating micro turbine intended for energy recovery in water supply networks. Their results highlighted the importance of including the tip clearance in the numerical simulations to get a better agreement with the experimental data. Fahlbeck et al. [13] showed numerical results of a CRPT with hydraulic efficiencies of close to 90% in both pump and turbine modes. These studies as well as the majority of available studies of CRPTs concern the blade design and steady-state operating conditions. However, unfavourable transient operating conditions are often responsible for most of the damage during turbine operation and have a direct negative effect on the lifetime of turbines [14].

In our recent research [15], preliminary startup and shutdown sequences for a model scale CRPT were studied. It was shown that

* Corresponding author.
E-mail addresses: fahlbeck@chalmers.se (J. Fahlbeck), hakan.nilsson@chalmers.se (H. Nilsson), saeed.salehi@chalmers.se (S. Salehi).

https://doi.org/10.1016/j.est.2023.106902
Received 16 June 2022; Received in revised form 17 January 2023; Accepted 13 February 2023
Available online 20 February 2023

the runners can experience large and rapid force and torque variations during the transient sequences in pump mode. Additionally, it was found that the pump mode startup is more severe than the shutdown for the evaluated sequence. Given that a PHS station may shift from pump mode to turbine mode several times a day, it is crucial to know how to optimally perform transient operations of the machine, for safety and to minimise premature deterioration [16].

An option for determining how to safely start up a CRPT in pump mode is to carry out an optimisation study of the transient startup sequence. A number of studies on optimisation of transients in pump-storage plants have recently been presented. As an example, Rezghi et al. [17] optimised the closing sequence of a wicket gate for a pump-turbine with 1D partial differential flow equations. The closing sequence was divided into a number of time segments, and a genetic algorithm (GA) was applied to minimise the runner over-speed and maximum over-pressure. Similarly, Liu et al. [18] used 1D flow equations to optimise the closing law of a wicket gate for a high-head PHS plant using a multi-objective optimisation GA. On the other hand, in the work by Mao et al. [19], computational fluid dynamics (CFD) was used to optimise a self-adaptive closure law during the load rejection sequence for a reversible pump-turbine. A multi-objective optimisation approach was adopted with the aim to decrease fluctuations in rotational speed and pressure. Furthermore, in the review paper by Kang et al. [20] on how to optimise for transient loads, it was suggested that for nonlinear and noisy data, response surface or surrogate-based optimisation (SBO) techniques can be used. In SBO, an approximate surrogate model is constructed based on sample points. The optimisation is then performed on the surrogate model, and not on the sampled data [21].

In the present work, an SBO approach is adopted using a GA to obtain an optimal solution. The surrogate is constructed based on CFD simulations of the pump mode startup sequences for a model scale CRPT within the ALPHEUS project. The aim of the optimisation study is to minimise loads (forces and torque) on the runners during the pump mode startup. The transient sequence includes a valve opening and speedup of the two individual runners. Five design variables are used to characterise the startup sequence and a single objective function is formalised based on the change of axial forces of the runners during the sequence. A design of experiment (DOE) matrix is constructed with a space-filling Latin hypercube sampling method [22], and a global single objective SBO [21] approach is used to find an optimal combination of the five variables.

The numerical framework includes 3D transient CFD simulations using the OpenFOAM-v2012 [23] open-source CFD code. The computational domain is limited to the region close to the runners and does not include the entire conduit. To include the main effects from the whole system that the CRPT is located in, the conduit and reservoirs are characterised by head losses at the boundaries of the computational domain using the headLossPressure boundary condition developed by Fahlbeck et al. [24]. A mesh study is performed to achieve an affordable, yet sufficiently accurate, low-fidelity (LoFi) CFD model for the many simulations of the optimisation study. The optimal solution is compared to a baseline case with the LoFi model. Finally, to verify the optimal startup sequence obtained with the LoFi model, the LoFi model is compared to a high-fidelity (HiFi) CFD model. Ultimately, this research contributes to increasing the knowledge of how to carry out transient operations of CRPTs with minimum load variation.

2. Pump-turbine design and operating conditions

The investigated CRPT with its conceptual mounting arrangement is shown in Fig. 1. In pump mode, the flow is from left to right (Runner 1 is upstream), and in turbine mode, it is from right to left (Runner 2 is upstream). The blade geometries were designed and optimised as part of the ALPHEUS project by Joseph et al. [25]. In this study, the CRPT is in model scale and has a shroud diameter of 27.6 cm and a hub diameter of 12.5 cm. The operating conditions of the model scale CRPT at the design point are summarised in Table 1 for both pump and turbine modes. The corresponding prototype scale is a 10 MW machine with a shroud diameter of up to 6 m. The two runners are connected to individual motors/generators and rotate independently of each other. Runner 1 has eight blades and Runner 2 has seven blades.

Table 1
Operating conditions of the model scale CRPT at the design point. Power, head and hydraulic efficiency are according to Fahlbeck et al. [15].

	Pump	Turbine	
Power (P)	55.4	16.7	kW
Net head[a] (H)	13.4	6.7	m
Flow rate (Q)	375.5	282.7	l/s
Hydraulic efficiency[b] (η)	88.5	90.3	%
Runner 1 (N_{R1})	1501.9	842.4	rpm
Runner 2 (N_{R2})	1129.1	633.3	rpm

[a]The head is based on the change in total pressure over CRPT.
[b]The efficiency is based on the net head of the CRPT.

The current study concerns the model scale CRPT since experimental studies will be carried out on the model scale as a part of the ALPHEUS project. In the future lab tests, the design point cannot be reached since the test facility consists of two open water reservoirs with limited possibilities to adjust the water levels. The reservoirs are connected with long pipes and the gross head of the open water surfaces can be set to 6.45 m, which is used in this study.

3. Optimisation properties

The optimisation procedure concerns the startup sequence in pump mode. The aim of the optimisation study is to minimise time-varying runner loads (axial force and torque) and peak loads on the runners. By minimising unfavourable load variations, the lifetime and flexibility of possible future PHS facilities may be extended since transient operations of hydraulic machines often cause the most hazardous events [14]. One option to decrease severe load variations is to perform the startup sequence very slowly, which is not desirable as it limits the machine's flexibility [26]. Hence, the maximum time of the startup sequence (t_{max}) is considered fixed and is set to 3 s in this work. In the startup sequence, the rotational speed of the two runners are individually increased and a valve is gradually opened. The flow field and performance of the machine are numerically analysed throughout the sequence with transient CFD simulations.

A single objective global SBO is performed in MATLAB (version R2021a) using GA [27,28]. The GA uses an evolutionary approach, where a new generation of samples is created based on mutating the best samples of the previous generation. In this work, the GA is configured to use a population size of 100 samples, and to continue creating offsprings until the relative change of the objective function for the best individual is converged below 10^{-8}. The GA presented a converged optimal solution within 53 generations.

Five design variables are used to characterise the transient sequence, which are the opening time of the valve ($t_{V,e}$), the speedup start times of Runner 1 and Runner 2 ($t_{R1,s}$ and $t_{R2,s}$), and the fraction of the remaining sequence for Runner 1 and Runner 2 (γ_{R1} and γ_{R2}). The fraction of the remaining time of the sequence is used to define the end time of the speedup of a runner as

$$t_{Ri,e}(t_{Ri,s}, \gamma_{Ri}) = t_{Ri,s} + (t_{max} - t_{Ri,s})\gamma_{Ri}. \quad (1)$$

Here, t_{max} is the maximum time of the sequence (3 s), index i is 1 or 2 for the respective runner, and subscripts 's' and 'e' represent the start and end times. The fraction variables (γ_{Ri}) allow all design parameters to be unconstrained and independent of each other.

For each design sample, the piecewise cubic Hermite interpolating polynomial [29] method is utilised to create a smooth time-variation

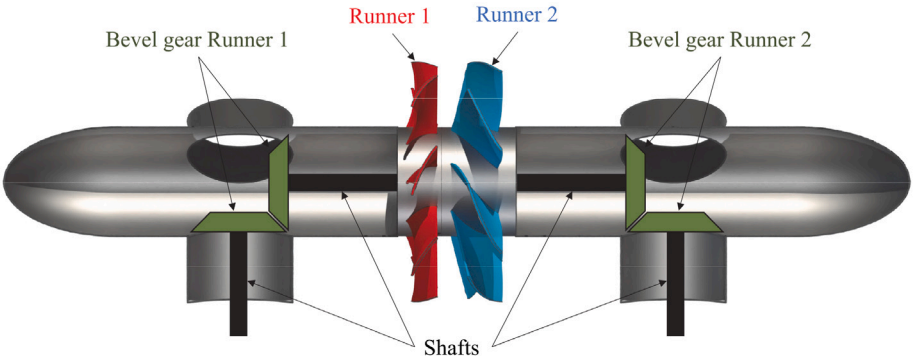

Fig. 1. Investigated CRPT and its conceptual mounting arrangement for the lab tests.

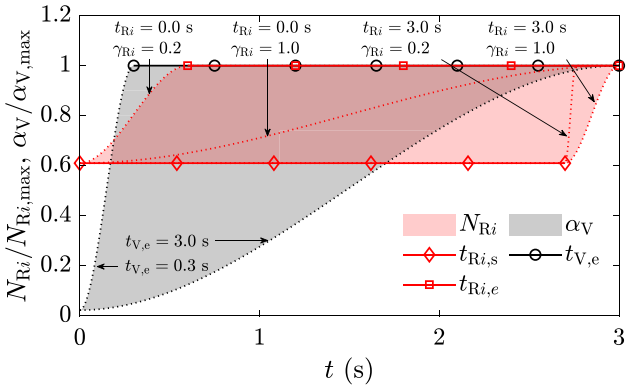

Fig. 2. Design space for the startup sequence, where N_{Ri} is the rotational speed of a runner and α_V is the valve opening. The dotted lines indicate the slowest and fastest possible valve opening or runner speedup at the edges of $t_{Ri,s}$ (see Section 3.2), and the shaded areas show all possible startup schemes. $N_{Ri,max}$ = 1501.9 rpm, and $\alpha_{V,max}$ = 90°.

for the valve opening and speedup of the runners, based on the calculated start and end times. The valve opening is controlled with a minor loss coefficient as explained in Section 4.2.

3.1. Startup sequence and design space

A PHS power plant is typically started in pump mode by speeding up the runner to its nominal rotational speed with a fully closed valve and then opening the valve (and guide vanes if applicable) [30]. Our experience suggests that such a procedure is not suitable for the CRPT configuration if a fast startup is desirable and if high-amplitude loads are to be avoided during the startup. Instead, the increase in the runner rotational speeds and valve opening need to be in joint operation for safe startup operation in pump mode.

The design space for the optimisation is depicted in Fig. 2. A value of 0 on the y-axis means that the valve (α_V) is closed or that there is no runner rotational speed (N_{Ri}), while a value of 1 refers to a fully open valve or the nominal runner rotational speed of 1501.9 rpm. The solid lines marked with ⋄ and ∘ indicate all possible times when initiating a runner speedup ($t_{Ri,s}$) and total valve opening times ($t_{V,e}$), respectively. The line marked with □ shows all possible end times of a runner speedup, obtained through Eq. (1). In the sequence, it is assumed that the rotational speeds of the runners are initially at 61% of their nominal rotational speed with a fully closed valve. That rotational speed is chosen through an extensive study to ensure that the net head produced by the machine matches the gross head of the facility that the machine is part of. This prevents reverse flow through the pump storage facility during startup. Our experience has shown that speeding up the runners to 61% of their respective nominal speed with a closed valve does not generate any severe loads. That part of the sequence is therefore excluded in the present study.

In each of the numerical simulations for the optimisation process, the flow field is fully developed prior to the commencement of the startup sequence. The valve starts to open at the initial time step, and continues to open until $t_{V,e}$. The rotational speeds of the runners independently increase from the initial values to their maximum between $t_{Ri,s}$ and $t_{Ri,e}$, where the latter is governed by γ_{Ri} and $t_{Ri,s}$ through Eq. (1). The simulations are continued with one additional second after the startup sequence, to reach fully developed conditions, yielding a total simulation time (t_{sim}) of 4 s.

3.2. Objective function

The goal of the optimisation study is to prevent severe load fluctuations with low frequency and high amplitude (force and torque for the whole runners and individual blades). Preliminary studies have shown that the load variations are largest when the change in axial force on the runners is largest. Therefore, it is suitable to minimise the time-integral of the magnitude of the gradient in time of the axial force, on both runners, to accomplish the goal. The objective function to be minimised is thus defined as

$$f(\boldsymbol{x}) = \int_{t=0}^{t_{sim}} \left(\left| \frac{\partial \bar{F}_{z,R1}(\boldsymbol{x})}{\partial t} \right| + \left| \frac{\partial \bar{F}_{z,R2}(\boldsymbol{x})}{\partial t} \right| \right) \mathrm{d}t, \tag{2}$$

for a design variable space given by (depicted in Fig. 2)

$$\begin{aligned} 0.3\ \text{s} \leq & t_{V,e} \leq 3.0\ \text{s}, \\ 0.0\ \text{s} \leq & t_{R1,s} \leq 2.7\ \text{s}, \\ 0.2 \leq & \gamma_{R1} \leq 1.0, \\ 0.0\ \text{s} \leq & t_{R2,s} \leq 2.7\ \text{s}, \\ 0.2 \leq & \gamma_{R2} \leq 1.0. \end{aligned} \tag{3}$$

Here, t_{sim} is 4 s which is the total time of each simulation (t_{max} + 1 s to ensure fully developed flow), $\bar{F}_z$ is the instantaneous averaged axial force and $\boldsymbol{x}$ is a vector of the five design variables $t_{V,e}$, $t_{R1,s}$, γ_{R1}, $t_{R2,s}$, γ_{R2}. The instantaneous average is obtained with a Savitzky–Golay finite impulse response filter [31], using a window size of 0.25 s.

An option could also be to include other terms such as the torque or force in the transverse directions in a similar fashion. However, by introducing more variables to the objective function, various weighting parameters also need to be added to scale the variables to a comparable level. The weighting factors would make the objective function more complex and our previous research [15] showed that the axial force and torque spikes appear at the same time. By minimising the proposed objective function it is ensured that large spikes and peaks are avoided.

3.3. Response surface

A Gaussian process (GP) regression model [32] is used to map the objective function into a response surface. A GP surrogate model is used since the objective function is non-linear and noisy. To assess the performance of the surrogate model, the leave-one-out cross-validation (LOOCV) is employed. In LOOCV each simulated data point is in turn excluded from the model training and used for validating the surrogate model that is generated without that sample [33]. The normalised root mean square error (nRMSE) [34],

$$\mathrm{nRMSE} = \frac{\sqrt{\frac{\sum_i^N \left(y_i - \hat{y}_i\right)^2}{N}}}{y_{\max} - y_{\min}}, \tag{4}$$

and R-squared (R^2) [21],

$$R^2 = \left[\frac{\mathrm{cov}(\boldsymbol{y}, \hat{\boldsymbol{y}})}{\sqrt{\mathrm{var}(\boldsymbol{y})\mathrm{var}(\hat{\boldsymbol{y}})}}\right]^2, \tag{5}$$

values are used to examine the accuracy of the surrogate model. Here y and $\hat{y}$ are the observed sample data and predicted data by the surrogate model, respectively, and N is the number of samples. In a GP surrogate model, it is assumed that the objective function $f(\boldsymbol{x})$ is distributed as a Gaussian process (Gaussian distribution for functions), as

$$f(\boldsymbol{x}) \sim \mathcal{GP}\left(m(\boldsymbol{x}), k(\boldsymbol{x}, \boldsymbol{x}')\right). \tag{6}$$

Here $m(\boldsymbol{x})$ is the mean function and $k(\boldsymbol{x}, \boldsymbol{x}')$ is the covariance function [35]. $\boldsymbol{x}'$ is any other value of the design parameters than $\boldsymbol{x}$. The covariance function is usually referred to as the kernel of the GP [36,37].

Several kernels are evaluated and the Matern 5/2 kernel [32,38], is the most promising for the used objective function. The Matern 5/2 kernel is defined as

$$k(\boldsymbol{x}, \boldsymbol{x}') = \sigma_s^2 \left(1 + \frac{\sqrt{5}r}{\ell} + \frac{5r^2}{3\ell^3}\right) \exp\left(-\frac{\sqrt{5}r}{\ell}\right), \tag{7}$$

where σ_s and ℓ are the signal standard deviation and characteristic length scale, while r represents the Euclidean distance between $\boldsymbol{x}$ and $\boldsymbol{x}'$ [39]. The variables σ_s and ℓ are called hyperparameters and can be optimised when training the regression model [32].

The GP surrogate model with the Matern 5/2 kernel achieves a LOOCV-nRMSE of 9.06% (Eq. (4)) and a LOOCV-R^2 value of 0.81 (Eq. (5)). The corresponding values without using the LOOCV method are an nRMSE of 4.32% and an R^2 of 0.96. The difference between the values when applying or not applying a LOOCV indicates that a LOOCV is required to get the true accuracy of the response surface without the risk of over-fitting. It is suggested by Sobester et al. [21] that a nRMSE < 10% is required for a reasonable prediction and that a surrogate model with an $R^2 > 0.8$ has good capabilities for predicting the true response. The predicted LOOCV values are just within the limits for an adequate response surface.

In the left graph of Fig. 3, the observed training data is compared to the estimated LOOCV response from the surrogate model. The predicted data shows an acceptable agreement with the observed training data, and most predicted points are within the standard deviation (σ) of the observed points. The standardised residual, is defined as

$$\mathrm{StR} = \frac{y_i - \hat{y}_i}{\sqrt{\mathrm{var}(\hat{\boldsymbol{y}})}},$$

is shown in the right graph of Fig. 3. Jones et al. [40] stated that the standardised residual should be within ±3 for a surrogate model to be valid. The value of ±3 approximately represents a 99.7% confidence interval [40]. The predicted data points show a sufficient standardised residual. The nRMSE, R^2 and the data fit graph provide confidence that the surrogate model can predict trends of the objective function to a great extent.

3.4. Sampling plan

The space-filling Latin hypercube sampling [22] method is used to sample the five design variables and distribute them onto a DOE matrix. The full DOE is divided into two stages. The first DOE contained 200 samples. Based on the results of the first DOE, 50 additional design points is evaluated in the area where the first DOE suggested that the optimal solution should be found. The design space of the additional DOE is constrained to

$$\begin{aligned}
1.5\ \mathrm{s} \leq & t_{\mathrm{V,e}} \leq 3.0\ \mathrm{s},\\
0.1\ \mathrm{s} \leq & t_{\mathrm{R1,s}} \leq 1.0\ \mathrm{s},\\
0.7 \leq & \gamma_{\mathrm{R1}} \leq 1.0,\\
1.5\ \mathrm{s} \leq & t_{\mathrm{R2,s}} \leq 2.5\ \mathrm{s},\\
0.7 \leq & \gamma_{\mathrm{R2}} \leq 1.0,
\end{aligned}$$

which can be compared to the design space of the first DOE, shown in Eq. (3).

The full DOE matrix used to predict the optimal startup sequence thus consists of 250 data points. Each data point represents a transient CFD simulation of the startup sequence. A single simulation is run using parallel processing with 32 CPU cores and requires roughly 10^3 core hours, see Section 4 for details about the numerical computations. Once all data points are evaluated with CFD, the data is post-processed to generate the objective function organised in a table with all the evaluated data points.

4. Numerical properties

OpenFOAM-v2012 is used for the transient CFD simulations. OpenFOAM [23,41] is an open-source object-oriented C++ code for CFD simulations. In the numerical simulations, the incompressible Reynolds averaged Navier–Stokes (RANS) equations are discretised and solved on a computational mesh using the finite volume method [42]. The eddy viscosity $k-\omega$ SST-SAS (shear stress transport-scale adaptive simulation) turbulence model is used for closure of the RANS equations. The SAS modifications to the traditional $k-\omega$ SST model allow for a local decrease in turbulent viscosity to resolve turbulence in parts of the computational domain [43,44]. The turbulence model has recently been used by several researchers in a hydropower context with sufficiently accurate results [45–50].

The numerical framework includes the full 3D computational domain shown in Fig. 4(a), and the results from the two meshes shown in Fig. 4(b) are compared in Section 5.2. The total length of the domain is 5.70 m (20.64 times the runner shroud diameter). The domain incorporates a hub, support struts, contraction/expansions before and after the machine, and straight pipes near the inlet and outlet of the domain. The full domain is divided into four regions, one for each runner and two regions up and downstream of the CRPT. The arbitrary mesh interface (AMI) technique is employed to transfer fluxes between the mesh regions [51,52]. The runners rotate individually by imposing time-varying solid body rotations according to the DOE samples.

4.1. Discretisation schemes and solver algorithm

Temporal discretisation is handled with the implicit second-order accurate backward scheme [53]. The time step is set to 2.5×10^{-4} s, which gives a maximum runner rotation per time step of 2.25° (at the nominal rotational speed). The time step is selected as a compromise between stability, accuracy, and the total time of each simulation. The maximum average Courant number [54] is around 0.16 and happens at the final operating condition.

The spatial discretisation schemes are of second-order accuracy for all variables except for the convection terms of the turbulent kinetic energy (k) and the specific turbulence dissipation rate (ω). For these variables, a first-order accurate upwind scheme is used. The convection

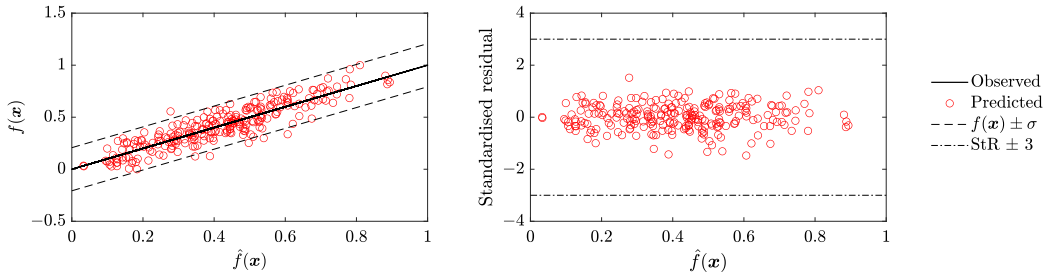

Fig. 3. Normalised observed sample points $f(\boldsymbol{x})$ (left) and standardised residual (right) as a function of normalised predicted LOOCV response $\hat{f}(\boldsymbol{x})$.

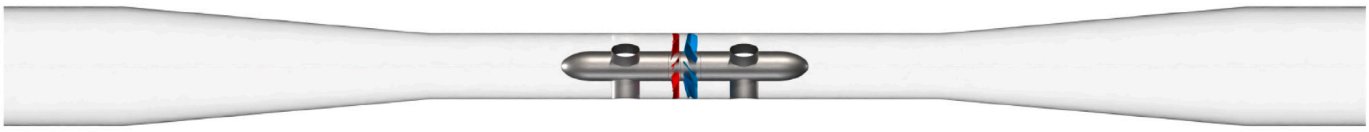

(a) Computational domain, flow is from left to right in pump mode

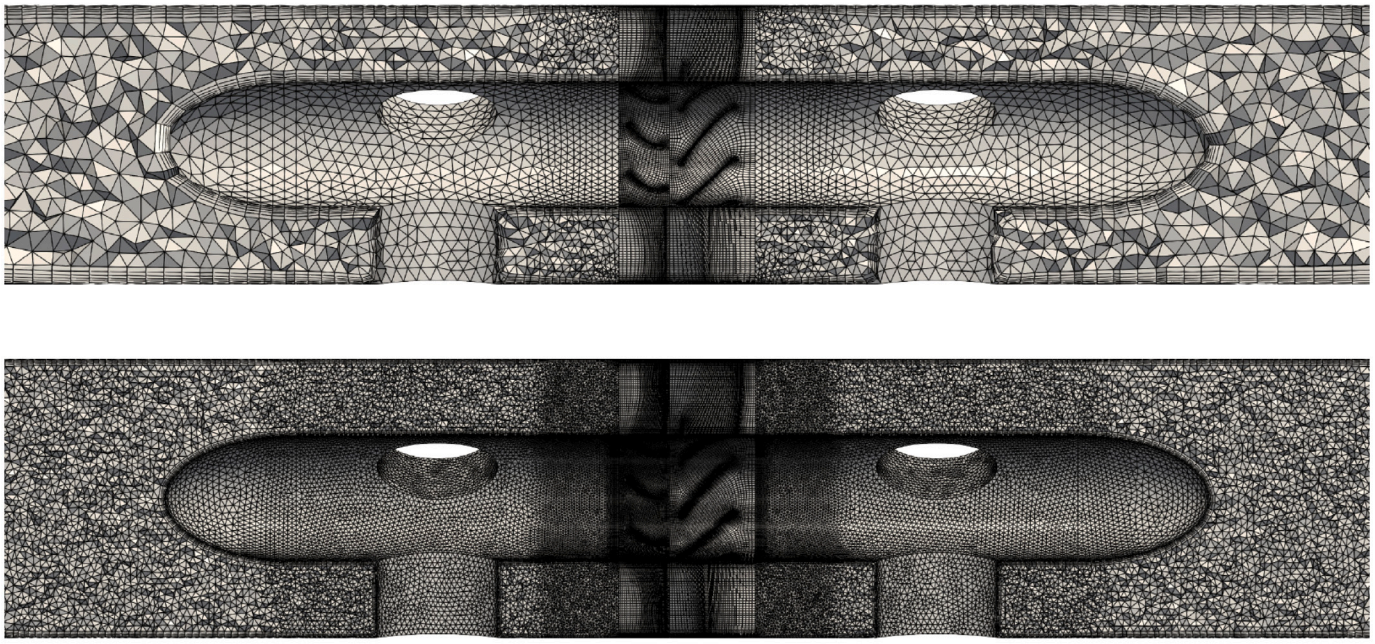

(b) Zoomed-in views of the LoFi (above) and HiFi (below) models meshes. See Section 5.2 for more details.

Fig. 4. Computational domain (a) and mesh (b) displayed in a cut view.

terms of the three velocity components are handled with the linear-upwind stabilised transport (LUST) scheme [55]. LUST is a blended scheme that employs 75% of a central difference scheme for accuracy, and 25% of a second-order upwind scheme for stability.

The OpenFOAM-v2012 pimpleFoam solver is used for all the simulations. It is a transient CFD solver for incompressible flows that utilises the PIMPLE algorithm [56]. This algorithm uses a pressure–velocity coupling that combines the PISO [57] and the SIMPLE [58] algorithms. PISO is used as an inner-loop corrector, while SIMPLE performs the outer-loop correction. The pimpleFoam solver is in this work configured with a maximum of 10 outer corrector loops per time step and two inner correction loops within every outer loop. One non-orthogonal corrector step is further performed at each inner loop. The outer corrector loop is interrupted when a specified convergence criterion is reached within the time step, and the simulation proceeds to the next time step. The convergence criterion is set to an absolute tolerance of 10^{-6} and 10^{-5}, or a relative solver tolerance of 0.01 and 0.001, for velocity and pressure, respectively. In OpenFOAM, the absolute tolerance is referred to as the solver residual, and the relative tolerance is the fraction of the final to initial residuals in the numerical solution loop of the linear system. In most time steps, a converged solution was obtained within four to six outer corrector loops.

4.2. Boundary conditions

For pressure, the headLossPressure boundary condition developed by Fahlbeck et al. [24] is used to achieve a flow-driving pressure difference over the computation domain. The flow rate is thus given as part of the solution. The boundary condition provides the possibility to include the main effects of pressure losses in the system caused by components such as valves, bends, pipe friction, etc, that are not considered in the computational domain. Thus, the pressure difference experienced by the CRPT in the simulations is caused by the computational domain and the system components that are not part of the simulation. The system is in this work configured according to the future lab tests that are to be made in the ALPHEUS project. Table 2 summarises the

Table 2
Input to the pressure boundary condition.

	Inlet	Outlet	
Surface elevation	3.25	9.70	m
Minor losses (loss coefficient)			
Bend	–	0.20	–
Sharp entrance	–	0.45	–
Sharp exit	1.00	–	–
Fixed valve	–	2×0.20	–
Opening valve	–	$k_V(\alpha_V, t)$	–
Friction losses			
Pipe length	1.00	15.50	m
Surface roughness	0.05	0.05	mm

prescribed head losses upstream and downstream of the computational domain. All minor loss coefficients and surface roughness of the pipes are taken from White [59], except the 'Opening valve', which is the valve that is being opened through the startup sequence using a smooth function, as described in Section 3. In the future experimental test facility, the valve is planned to be located far downstream of the CPRT in pump mode. Hence, the valve will have a limited effect on the flow field by the runners.

The relation between the minor loss coefficient of the valve, k_V, and its opening angle, α_V, is estimated based on data provided by the test facility as

$$k_V(\alpha_V) = \exp(-4.2351 \ln(\alpha_V) + 18.1149). \tag{8}$$

The valve is of a butterfly type where 90° represents the fully open state while 0° indicates the fully closed position. Due to numerical instability, the valve cannot be fully closed in the simulations, as the minor loss approaches infinity when the opening is 0° (see Eq. (8)). Therefore, the smallest opening angle used in the simulations is 2°, which gives a minor loss coefficient of $k_V(2) = 3.91 \times 10^6$, yielding a negligible flow rate at this opening.

The pressureInletOutletVelocity [23] boundary condition is used at both the inlet and the outlet for the velocity. This boundary condition prescribes a zero-gradient (homogeneous Neumann) condition, with the restriction that inflow is only allowed in the face-normal direction. All walls are treated with the no-slip condition and wall functions are used to model wall viscous effects.

4.2.1. Mesh study and chosen mesh

In the optimisation study, several hundreds of simulations of transient sequences should be carried out. It is thus necessary to have an affordable computational model while still capturing the essential physical trends accurately. Thus, a mesh study is performed to estimate the discretisation error of a coarse CFD model. Five different mesh sizes are evaluated at a fixed operating point, with total cell counts of 21.32, 9.76, 5.02, 2.36, and 1.15 million cells, respectively. Time-averaged values of the CRPT power (P) using these meshes are shown as a function of average cell size in Fig. 5. The average cell size is computed as

$$h = \left(\frac{1}{N} \sum_{i}^{N} \Delta V_i \right)^{1/3}, \tag{9}$$

where N is the number of cells and ΔV_i is the volume of the ith cell. Discretisation schemes and boundary conditions are identical for all the cases in the mesh study. However, the time step is varied so that the average Courant number [54] is kept as close as possible for the different mesh sizes.

Richardson extrapolation (RE) is performed on the CRPT power given by the three finest meshes to estimate the numerical discretisation error [60,61]. The grid convergence index ($\mathrm{GCI}^{\mathrm{fine}}$), the extrapolated relative error ($e_{\mathrm{ext}}^{\mathrm{fine}}$) of the finest mesh ($21.32 \times 10^6$ cells), and the extrapolated relative error ($e_{\mathrm{ext}}^{\mathrm{coarse}}$) of the coarsest mesh ($1.15 \times 10^6$ cells)

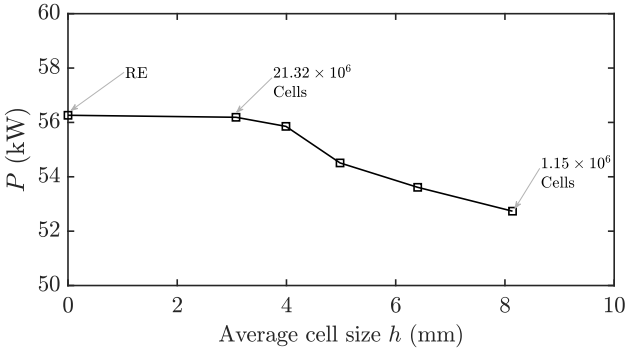

Fig. 5. Power as a function of average cell size h.

are 0.16%, 0.13% and 6.27%, respectively. The extrapolated values suggest that the discretisation error of the finest mesh is less than 0.2%. The present study however focuses on the coarsest mesh with 1.15×10^6 cells (referred to as the LoFi model) and the mesh with 9.76×10^6 cells (referred to as the HiFi model). See Fig. 4(b) for a graphical view of those meshes. The LoFi model falls outside the asymptotic range of convergence. However, the HiFi model is well within this range since

$$\frac{\mathrm{GCI}^{\mathrm{HiFi}}}{r^p \mathrm{GCI}^{\mathrm{fine}}} = 1.000.$$

Furthermore, the HiFi model achieves a $\mathrm{GCI}^{\mathrm{HiFi}}$ of 0.90%, and a $e_{\mathrm{ext}}^{\mathrm{HiFi}}$ of 0.72%. This means that the expected discretisation error of the HiFi model is less than 1%. Therefore, the HiFi model results are in Section 5.2 used to validate the results of the LoFi model during a full transient sequence. Although the relative error of the LoFi model is larger, and that it falls outside the asymptotic range of convergence, the validation shows that it gives acceptable results for the optimisation process. The power is only underestimated by a few percent, and the mesh is fine enough to capture the most essential physics during the transient sequence. At the same time, the LoFi mesh is coarse enough to make the optimisation study feasible. Therefore, considering the fact that hundreds of CFD simulations of transient sequences need to be performed, the coarse mesh with 1.15×10^6 cells is chosen for the optimisation study.

As described earlier, and as can be seen in Fig. 4(b), the computational mesh is divided into four parts, one for each runner and one for each of the two regions upstream and downstream the CRPT. The runner meshes are block-structured, except in the tip-clearance region where four layers of hexahedral and triangular prism cells are used. The upstream and downstream regions consist of six prism boundary layer cells and unstructured tetrahedral core cells. The mesh is finest close to the runners and is gradually coarser further away. The total cell count is 1.15×10^6 cells. The mesh regions of Runners 1 and 2 contain 0.35×10^6 and 0.28×10^6 cells, respectively, while the upstream and downstream regions contain 0.26×10^6 cells each. The average y^+ value of the first nodes at the walls is between 40–210.

5. Results and discussion

The outcome of the optimisation study is presented and discussed in this section. The optimal solution is compared to a baseline startup sequence in Section 5.1. For the baseline case, the valve gradually opens up during the whole three seconds. Simultaneously, both runners utilise the full time of the sequence to steadily speed up. Additionally, the optimal startup sequence, estimated with the LoFi model, is validated using the results of a HiFi model in Section 5.2. Flow structures during the optimised startup sequence are finally examined in Section 5.3 with the HiFi model. Recall that the maximum time of the startup sequence ($t_{\max}$) is 3 s. However, in the graphs presented in this section, one

additional second is added to show the developed conditions at the final operating point. Furthermore, all the force and torque graphs show smoothed instantaneous average values. See Section 3.2 for further details about the smoothing procedure.

5.1. The optimal startup sequence

The optimal startup sequence suggested by the optimisation algorithm is shown together with the baseline sequence in Fig. 6. The optimal and baseline design variables and the objective function are summarised in Table 3. In the optimal startup sequence, Runner 1 (upstream) starts speeding up prior to Runner 2 (downstream), and there is an overlap between the speedup procedures of the two runners. The Runner 1 speedup time is 2.728 s, which corresponds to 91% of the entire sequence. The speedup of Runner 2 is faster and requires only 0.890 s, which corresponds to 30% of the entire sequence. The valve opens up during 73% of the sequence. Moreover, the valve is almost fully opened prior to the speedup of Runner 2, while there is a large overlap between the valve opening and the speedup of Runner 1 in the optimal sequence. Comparing the observed, $f(\boldsymbol{x})$, and estimated, $\hat{f}(\boldsymbol{x})$, objective functions reveals that the surrogate model manages to predict the objective function adequately with an acceptable relative error of 3.5% for the optimal case and 6.6% for the baseline case.

To verify that the optimised startup sequence indeed is a favourable alternative, the loads on the runners are compared to those of the baseline startup sequence in Fig. 7. Also, the average plus/minus the standard deviation of the first 200 DOE samples at each time step is shown. The first 200 DOE samples are used since they are statistically independent. Recall that the axial force and torque are smoothed in the graphs, thus only the main variation is demonstrated. Focusing on the variation of axial force (left graph in Fig. 7), it is shown that Runner 2 may experience larger detrimental force oscillations, which can be explained by the fact that complex flow structures leaving Runner 1 encounter Runner 2. The maximum encountered axial force (left graph) and torque (right graph) for all the evaluated sequences surpass values of 6.5 kN and 360 N m, respectively. The optimal solution shows remarkably lower peaks for the force and torque. The load variation for Runner 2 shows a rather smooth behaviour for the optimised solution, whereas a clear peak arises around $t = 1.7$ s for the baseline case. The peak load of the baseline case at 1.7 s is in fact outside of the standard deviation, which indicates that a random startup sequence should in principle be a better alternative than the baseline sequence. However, as seen by the maximum force and torque of all the evaluated samples, a random sample could also be a less favourable alternative. The variation of axial force and torque of Runner 1 for the optimal case does not show any significant improvements compared to the baseline alternative. However, the loads on Runner 1 are generally smaller than on Runner 2, indicating the importance of the Runner 2 loads for the CRPT machine.

Table 3
Design variables and objective function for the optimal and baseline sequences.

Variable	$t_{V,e}$	$t_{R1,s}$	γ_{R1}	$t_{R2,s}$	γ_{R2}	$f(\boldsymbol{x})$	$\hat{f}(\boldsymbol{x})$
Optimal	2.179 s	0.223 s	0.982	2.030 s	0.917	9.811	10.167
Baseline	3.000 s	0.000 s	1.000	0.000 s	1.000	11.617	12.438

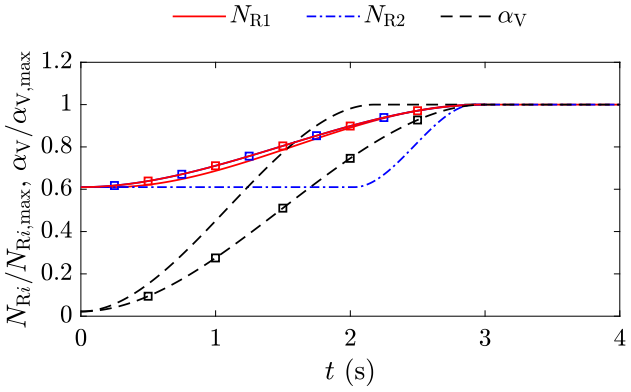

Fig. 6. Optimal and baseline startup sequences as a function of time. The baseline sequence is indicated with □ markers, note that the runner speedups are identical for the baseline. $N_{Ri,max} = 1501.9$ rpm, and $\alpha_{V,max} = 90°$.

Decreasing the low-frequency high-amplitude fluctuations of forces and torques on the full runners, the machine lifetime increases and the likeliness of total breakdown of the machine due to fatigue reduces. The hydraulic loads on the full runners indicate the main loads transmitted to the mechanical system, e.g., shafts, bearings, support structures, etc. For axial-flow machines where the blades are not supported by the shroud, it can also be important to monitor loads on a single blade since all oscillations might not be detectable on the full runner as the blade loads can potentially cancel each other out. The axial forces and torques shown in Fig. 8 are evaluated for a single blade on each runner. The single-blade load variation is closely connected to the lifetime of the runner itself. Persistent large spikes may lead to fatigue or even breakdown of the runner blades. The optimal solution shows no severe force or torque spikes. The torque is in fact showing a fairly smooth variation during the startup for the optimal case. In contrast, the Runner 2 curves of the baseline sequence present notable axial force and torque peaks that exceed the loads at the final operating point.

The time variation of the flow rate during the startup, demonstrated in Fig. 9, can also explain the advantageous performance of the optimal case. The optimal solution presents a gradual increase in flow rate through most of the sequence, while the baseline case shows more abrupt changes. A distinct change in the rate of increasing flow rate appears for the baseline case around $t = 1.8$ s, shortly after the Runner 2 peaks in axial force and torque, shown in Figs. 7 and 8. The variation of flow rate indicates that a safe startup sequence cannot be achieved without a smooth and gradual increase in the flow rate.

The significant differences between the Runner 2 loads of the optimal and baseline cases at roughly $t = 1.7$ s are further investigated through the tangential velocity and secondary flow vectors in Fig. 10.

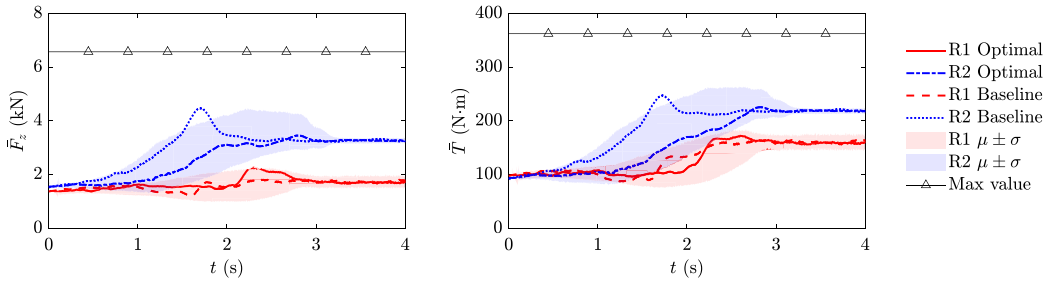

Fig. 7. Axial force (left) and torque (right) for the full runners as a function of time. The shaded areas show the mean (μ) ± the standard deviation (σ) at each time step for the first 200 DOE samples. The max value is the maximum value encountered for all the evaluated sequences.

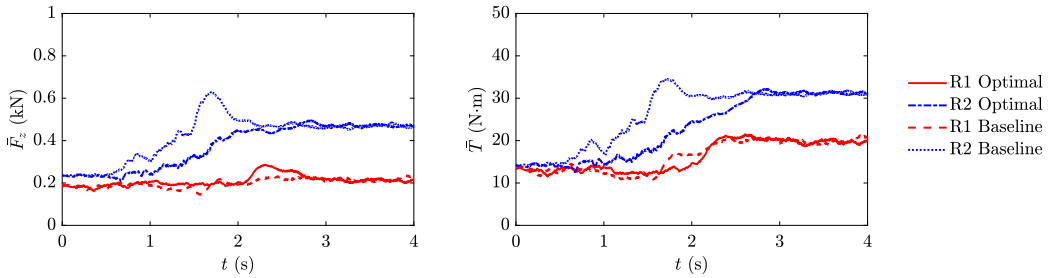

Fig. 8. Axial force (left) and torque (right) of a single blade for both runners as a function of time.

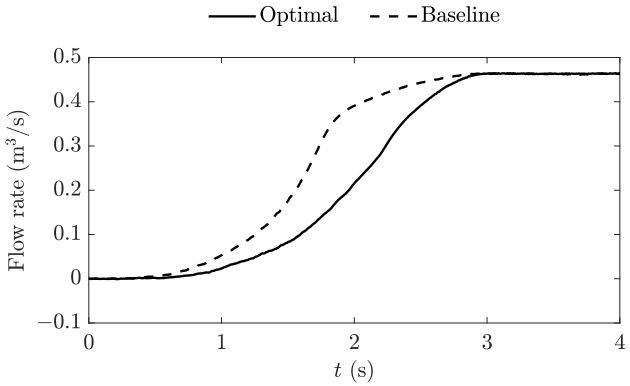

Fig. 9. Flow rate as a function of time.

The results are from the HiFi CFD model (9.76×10^6 cells and $\Delta t = 5{\times}10^{-5}$ s), which is discussed in detail in Section 5.2. In each subfigure, the left picture illustrates the flow field between the runners while the right one represents the flow field downstream of Runner 2 (the red and blue planes in Fig. 10(g), respectively). The secondary flow vectors between the runners for the optimal case at $t = 1.5$ s, shown in Fig. 10(a) (left figure) indicate a non-uniform flow. Furthermore, the tangential velocity contour suggests mostly a clockwise swirl ($u_\theta > 0$) direction between the runners. After Runner 2 (right figure), a counter-clockwise swirl ($u_\theta < 0$) can be observed. A counter-clockwise swirl downstream of Runner 2 is also encountered for the baseline case at $t = 1.5$ s (right picture in Fig. 10(b)). At the same time, compared to the optimal case, a more uniform clockwise swirl is formed between the two runners in the baseline case. Moreover, the flow rate is larger for the baseline case at $t = 1.5$ s, which means that a larger torque is required to change the flow direction. Therefore, the abrupt changes in the flow swirl direction, in combination with the higher flow rate, can be seen as another physical explanation of the large load fluctuations on Runner 2 in the baseline case, which are considerably reduced by the optimisation procedure.

Later on, the secondary flow patterns of the optimal case in Figs. 10(c) and 10(e) indicate an increase of the tangential velocity between the runners. On the other hand, the secondary flow direction after Runner 2 demonstrates no drastic changes between $t = 1.6$ and 1.7 s. This is because, based on the optimal operation, the rotational speed of Runner 1 increases, while the rotational speed of Runner 2 does not. The same analysis for the baseline case (Figs. 10(d) and 10(f)) suggests that the magnitude of the tangential velocity between the runners is smaller than for the optimal case. However, the secondary flow vectors indicate that the direction is more aligned in a clockwise direction. The flow after Runner 2 shows a counter-clockwise direction for the baseline case with comparably small values of tangential velocity at $t = 1.7$ s. Additionally, at the final time step, traces of wakes from Runner 1 are visible between the runners for the baseline case as an effect of the larger flow rate and the more ordered flow. Similar patterns are apparent for the optimal case at later time steps as well.

The combination of a comparably high flow rate, a dominant clockwise swirl between the runners, and a distinct counter-clockwise swirl downstream of Runner 2 explains the load peaks for the baseline case at $t \approx 1.7$ s, shown in Figs. 8 and 9. This is because Runner 2 is responsible for the torque required to change the flow direction from clockwise to counter-clockwise. For the optimal case, there are larger values of the tangential velocity between the runners. However, the secondary flow vectors show that the flow swirl direction is less ordered for the optimal case than for the baseline case. Moreover, the flow rate is smaller in the optimal case, which means that the CRPT is working more like a mixer than a pump at the evaluated time steps.

To further explain why the optimal case reduces the undesirable load peaks compared to the baseline case, the axial component of the angular momentum flux over Runner 2 is shown in Fig. 11. The angular momentum flux is derived from Reynolds' transport theorem [59], and uses a control volume approach by applying conservation of angular momentum as

$$\boldsymbol{M} = \iint_S (\boldsymbol{r} \times \boldsymbol{u})\rho(\boldsymbol{u} \cdot \boldsymbol{n})\,\mathrm{d}S \quad \Rightarrow \quad M_z = \iint_S (ru_\theta)\rho(\boldsymbol{u} \cdot \boldsymbol{n})\,\mathrm{d}S. \tag{10}$$

Here, $\boldsymbol{r}$ is the lever vector (r is the lever in the radial direction), ρ is the fluid density, S is the control volume surfaces, $\boldsymbol{u}$ is the velocity vector, $\boldsymbol{n}$ is the surface normal vector and subscript θ denotes the tangential direction. The equation is a general form of the Euler turbine equation, $T = \dot{m}(r_2 u_{\theta 2} - r_1 u_{\theta 1})$, and describes the change of angular momentum over a control volume. The control volume surfaces are in this case defined according to the red and blue surfaces in Fig. 10(g).

The curve for the baseline case in Fig. 11 shows a peak value at $t \approx 1.7$ s, which is at the same time as the axial force and torque peaks occur. Hence, the high Runner 2 load peaks for the baseline case are caused by the change in tangential velocity over the runner, while at the same time having a significant flow rate. This is because Eq. (10) in principle demonstrates the change of tangential velocity over the control volume multiplied by the flow rate, since the average lever is constant. For the optimal case, no distinct peak is demonstrated.

5.2. Verification of the optimal startup sequence

To verify that the performance of the optimal solution, based on the LoFi CFD model (coarse mesh with $1.15{\times}10^6$ cells and $\Delta t = 2.5{\times}10^{-4}$ s), is as promising as suggested in Section 5.1, the optimal sequence is numerically analysed with the HiFi CFD model (fine mesh with 9.76×10^6 cells and $\Delta t = 5 \times 10^{-5}$ s). In Fig. 4(b), a visual comparison of the LoFi and HiFi computational meshes is displayed. For the HiFi model, all solver settings are identical to the LoFi model, except the time step which is decreased for numerical stability and increased accuracy. The LoFi model requires roughly 1×10^3 CPU core hours for the startup sequence, while the HiFi model needs 50×10^3 CPU core hours. The LoFi model is thus around 50 times less computationally demanding, which is why it was used for the optimisation study.

In Fig. 12, the axial force and torque are compared between the HiFi and LoFi models. The LoFi model manages to predict the trends

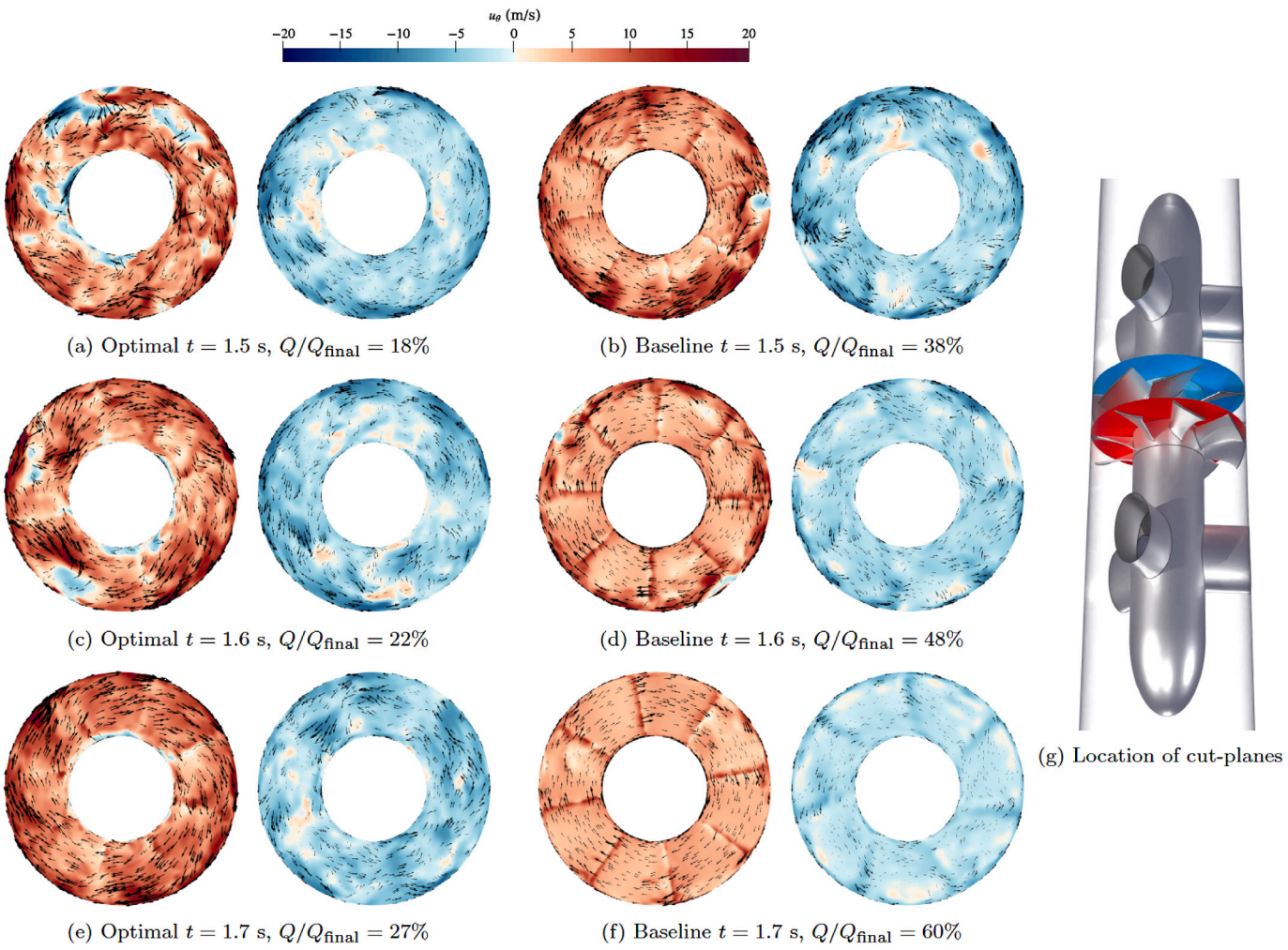

Fig. 10. Contours of tangential velocity and in-plane vectors of secondary flow (scaled with the velocity magnitude) at two cut-planes for the optimal and the baseline cases at various times. The lower cut-plane is located between the runners (red plane in g) and the above plane is placed downstream of Runner 2 (blue plane in g). (For interpretation of the references to colour in this figure legend, the reader is referred to the web version of this article.)

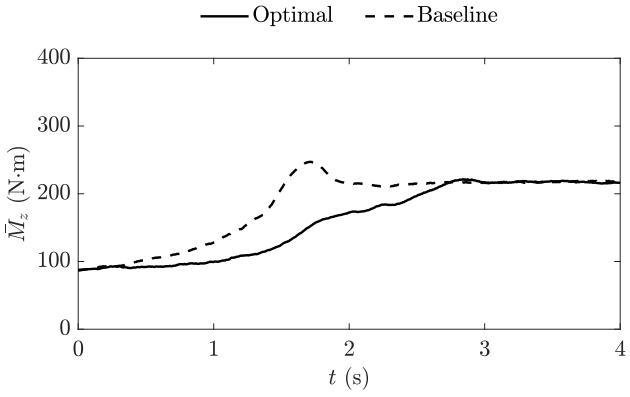

Fig. 11. Axial component of the angular momentum flux (Eq. (10)) over Runner 2 as a function of time.

of the sequence rather well since the curves of the HiFi and LoFi models are similar. There are nonetheless some inevitable differences. The LoFi model mostly under-predicts the Runner 1 loads, while for Runner 2, the loads are over-predicted. In the LoFi case, this results in that the downstream runner is to a larger extent responsible for generating the required head. The predicted head is almost the same for the LoFi and HiFi models and can be translated to the sum of axial force (R1 + R2 in the left graph of Fig. 12). The sum of torque is in general under-predicted by the LoFi model, which has a decisive impact on the computed flow rate.

The increase in flow rate for the HiFi and LoFi models of the optimised startup sequence is shown in Fig. 13. The general trend is captured by the LoFi model. However, there is an offset starting at $t \approx 0.5$ s. Also, at the later time steps the LoFi model under-predicts the flow rate by roughly 5%. The offset at the later time steps is explained by the smaller torque estimated by the LoFi model, as shown in Fig. 12 (R1 + R2 in the right graph). A smaller torque put into the flow means less momentum to generate the pressure increase by the CRPT that drives the flow through the computational domain. The underestimation of torque is most likely caused by the fact that a large part of the wall viscous effects is modelled through wall functions in the computational domain for the LoFi model, whereas the HiFi model resolves a larger part of the boundary layers.

The results from the HiFi model demonstrate a similar behaviour as the LoFi model for the optimised startup sequence in pump mode. This implies that the sample points generated by the LoFi model can adequately predict the physical phenomena behind the damaging effects of the startup sequence. Additionally, the GP surrogate model and the SBO obtained with the GA can present an optimal combination of the design variables to avoid drastic low-frequency, high-amplitude, load peaks and thus limit the risk of fatigue and total breakdown.

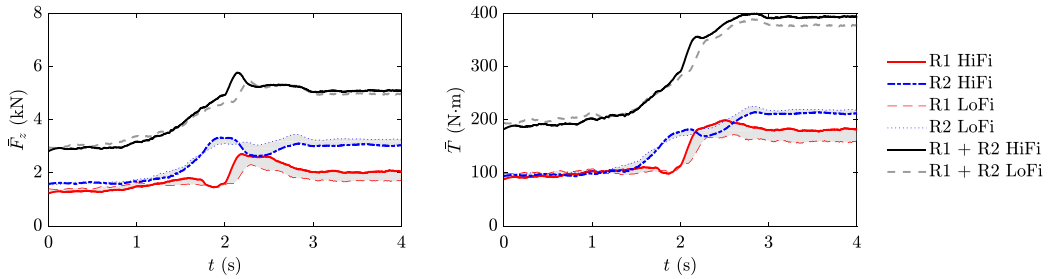

Fig. 12. Axial force (left) and torque (right) for the full runners as a function of time. The shaded areas indicate the difference between the HiFi and the LoFi models.

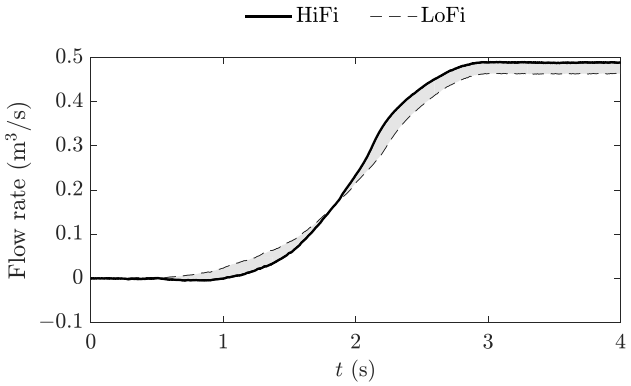

Fig. 13. Flow rate as a function of time, the shaded area indicates the difference between the HiFi and LoFi models.

5.3. Flow structures during the optimised startup sequence

Iso-surfaces of the λ_2-criterion [62] with the HiFi model are demonstrated in Fig. 14, to study the complex flow structures during the optimal startup sequence. At $t = 0.5$ s (Fig. 14(a)) the machine is mainly working as a mixer, due to a near-zero flow rate. Most of the flow structures are centred around Runner 1, indicating massively separated flow near this runner. At $t = 1.5$ s (Fig. 14(b)) the flow rate has started to increase because of the rising rotational speed of Runner 1 and the opening of the valve. This causes larger flow structures around both runners. The flow rate is still far from the final operating condition, resulting in a heavily separated flow field around the blades.

Recall the rapid change in axial forces and torques, shown in Fig. 12, close to $2.0 < t < 2.2$ s. Figs. 14(c)–14(e) show that the flow undergoes a significant change between $t = 2.0$ to 2.2 s. The flow is transformed from being mainly mixed by the runners, to having a more developed behaviour. Most of the small flow structures between the runners are diminished during this short period, and tip clearance vortices at the leading edge of the runner blades are seen at $t = 2.2$ s.

The tip clearance vortices are still apparent at the final time step of the startup sequence, at $t = 3.0$ s, as shown in Fig. 14(f). Additionally, vortex shedding from the upstream support struts is developed. Traces of vortex shedding for the downstream support struts are also found. However, a smaller λ_2 value is required to clearly visualise the downstream support struts vortex shedding. The value of $\lambda_2 = 5 \times 10^5$ s^{-2} was chosen to visualise flow structures close to the runners rather than in the whole computational domain.

6. Conclusions

The current study has successfully demonstrated an approach for reducing flow-induced load pulsations during a transient startup sequence for a CRPT in pump mode. The startup scheme is based on the rotational speed of the runners being set to initial values with a closed valve, so that the net head of the CRPT matches the gross head of the PHS facility. This ensures a minimal energy loss for the PHS station during startup since reverse flow from the upper to the lower reservoir is avoided.

The developed optimisation framework is configured to minimise, low-frequency, high-amplitude load pulsations during the transient startup sequence. In the sequence, the valve starts to open up at the initial time step, and the runners' rotational speeds gradually increase. The maximum allowed time of the startup sequence is set to 3 s, and five design variables that control the startup sequence are optimised. One variable is used for the valve and two for each of the runners.

The optimisation algorithm suggests that the valve should be fully open after 73% of the full time of the sequence. The speedup of Runner 1 (upstream) should start prior to that of Runner 2 (downstream), and Runner 1 should speed up during most of the sequence. The speedup of Runner 2 should be almost three times as fast as that of

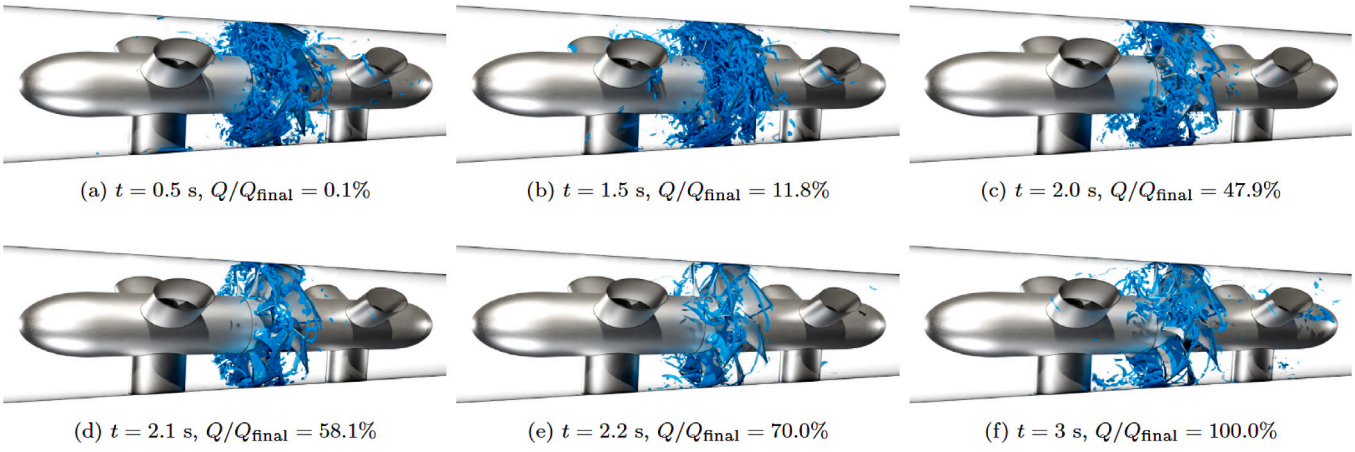

Fig. 14. Iso-surfaces of $\lambda_2 = 5 \times 10^5$ s^{-2} with the HiFi model during the optimal startup sequence at various time steps. Note that the flow is from left to right.

Runner 1, and its increase in rotational speed should occur during the final third of the sequence.

The optimal startup sequence shows a smooth increase in the flow rate through the sequence. A smooth change in flow rate during the startup reduces drastic peak values of torque and axial force of both the full runners and also a single blade on each runner. The machine may experience numerous startup sequences throughout its lifetime, and the risk of fatigue and total breakdown of the runner blades are reduced by limiting the drastic load peaks.

For possible future PHS stations with CRPTs, it is recommended to execute transient operations in pump mode that ensures a smooth variation in the change of flow rate throughout the transient. By monitoring the change in flow rate, it should possible to carry out further optimisation studies on transient operations. Such studies can use a similar strategy as the one presented in this paper. Simplified models, with e.g. characteristics of the pump-turbine, could potentially also be used.

CRediT authorship contribution statement

Jonathan Fahlbeck: Conceptualization, Methodology, Software, Validation, Formal analysis, Investigation, Writing – original draft, Writing – review & editing, Visualization, Project administration. **Håkan Nilsson:** Conceptualization, Resources, Writing – review & editing, Supervision, Funding acquisition. **Saeed Salehi:** Conceptualization, Formal analysis, Writing – review & editing, Supervision.

Declaration of competing interest

The authors declare that they have no known competing financial interests or personal relationships that could have appeared to influence the work reported in this paper.

Data availability

The authors do not have permission to share data.

Acknowledgements

This project has received funding from the European Union's Horizon 2020 research and innovation programme under grant agreement No. 883553. The computations were enabled by resources provided by the Swedish National Infrastructure for Computing (SNIC) at NSC and C3SE, partially funded by the Swedish Research Council through grant agreement No. 2018-05973. All authors approved the version of the manuscript to be published.

References

[1] H.E. Murdock, D. Gibb, T. Andre, J.L. Sawin, A. Brown, L. Ranalder, T. Andre, A. Brown, U. Collier, C. Dent, B. Epp, C. Hareesh Kumar, F. Joubert, R. Kamara, N. Ledanois, R. Levin, J. Skeen, F. Sverrisson, G. Wright, F. Passaro, F. Guerra, N.M. Dwi Sastriani, H. Yaqoob, S. Gicquel, V. Hamirwasia, G. Kifukwe, Y. Yuan-Perrin, T. Mayer, L.E. Williamson, A. Budiman, O. Chen, K. Findlay, A. Harris, J. Jones-Langley, F. Urbani, L. Mastny, L. Brumer, Renewables 2021 - Global status report, INIS-FR–21-0788, REN21, 2021, p. 603.

[2] J.P. Hoffstaedt, D.P.K. Truijen, J. Fahlbeck, L.H.A. Gans, M. Qudaih, A.J. Laguna, J.D.M. De Kooning, K. Stockman, H. Nilsson, P.-T. Storli, B. Engel, M. Marence, J.D. Bricker, Low-head pumped hydro storage: A review of applicable technologies for design, grid integration, control and modelling, Renew. Sustain. Energy Rev. 158 (2022) 112119, http://dx.doi.org/10.1016/j.rser.2022.112119.

[3] V. Kitsikoudis, P. Archambeau, B. Dewals, E. Pujades, P. Orban, A. Dassargues, M. Pirotton, S. Erpicum, Underground pumped-storage hydropower (UPSH) at the martelange mine (Belgium): Underground reservoir hydraulics, Energies 13 (14) (2020) 3512, http://dx.doi.org/10.3390/en13143512.

[4] ALPHEUS H2020, 2022, URL https://alpheus-h2020.eu/ accessed on 17 February 2023.

[5] M. Qudaih, B. Engel, D. Truijen, J.D. Kooning, K. Stockman, J. Hoffstädt, A. Jarquin-Laguna, R.A. Ruiz, N. Goseberg, J. Bricker, J. Fahlbeck, H. Nilsson, L. Bossi, M. Joseph, M. Zangeneh, The contribution of low-head pumped hydro storage to a successful energy transition, in: Proceedings of the Virtual 19th Wind Integration Workshop, 2020.

[6] J. Carlton, Marine Propellers and Propulsion, Butterworth-Heinemann, 2018.

[7] R. Ansorena Ruiz, L.H. de Vilder, E.B. Prasasti, M. Aouad, A. De Luca, B. Geisseler, K. Terheiden, S. Scanu, A. Miccoli, V. Roeber, M. Marence, R. Moll, J.D. Bricker, N. Goseberg, Low-head pumped hydro storage: A review on civil structure designs, legal and environmental aspects to make its realization feasible in seawater, Renew. Sustain. Energy Rev. 160 (2022) 112281, http://dx.doi.org/10.1016/j.rser.2022.112281.

[8] J.-H. Kim, B.-M. Cho, S. Kim, J.-W. Kim, J.-W. Suh, Y.-S. Choi, T. Kanemoto, J.-H. Kim, Design technique to improve the energy efficiency of a counter-rotating type pump-turbine, Renew. Energy 101 (2017) 647–659, http://dx.doi.org/10.1016/j.renene.2016.09.026.

[9] J.-W. Kim, J.-W. Suh, Y.-S. Choi, K.-Y. Lee, T. Kanemoto, J.-H. Kim, Optimized blade design of counter-rotating-type pump-turbine unit operating in pump and turbine modes, Int. J. Rotating Mach. (2018) http://dx.doi.org/10.1155/2018/6069780.

[10] E. Vagnoni, L. Andolfatto, S. Richard, C. Münch-Alligné, F. Avellan, Hydraulic performance evaluation of a micro-turbine with counter rotating runners by experimental investigation and numerical simulation, Renew. Energy 126 (2018) 943–953, http://dx.doi.org/10.1016/j.renene.2018.04.015.

[11] W. Xiuli, L. Bin, L. Yang, Z. Yan, Z. Rongsheng, L. Yun, F. Qiang, Hydraulic optimization of two-way counter-rotating axial flow pump turbine, Front. Energy Res. 8 (2020) http://dx.doi.org/10.3389/fenrg.2020.577232.

[12] R. Subbarao, M. Govardhan, Identification of flow physics in a counter rotating turbine, J. Appl. Fluid Mech. 13 (3) (2020) 767–777.

[13] J. Fahlbeck, H. Nilsson, S. Salehi, M. Zangeneh, M. Joseph, Numerical analysis of an initial design of a counter-rotating pump-turbine, IOP Conf. Ser.: Earth Environ. Sci. 774 (1) (2021) 012066, http://dx.doi.org/10.1088/1755-1315/774/1/012066.

[14] X. Liu, Y. Luo, Z. Wang, A review on fatigue damage mechanism in hydro turbines, Renew. Sustain. Energy Rev. 54 (2016) 1–14, http://dx.doi.org/10.1016/j.rser.2015.09.025.

[15] J. Fahlbeck, H. Nilsson, S. Salehi, Flow characteristics of preliminary shutdown and startup sequences for a model counter-rotating pump-turbine, Energies 14 (12) (2021) 3593, http://dx.doi.org/10.3390/en14123593.

[16] U. Seidel, C. Mende, B. Hübner, W. Weber, A. Otto, Dynamic loads in Francis runners and their impact on fatigue life, IOP Conf. Ser.: Earth Environ. Sci. 22 (3) (2014) 032054, http://dx.doi.org/10.1088/1755-1315/22/3/032054.

[17] A. Rezghi, A. Riasi, P. Tazraei, Multi-objective optimization of hydraulic transient condition in a pump-turbine hydropower considering the wicket-gates closing law and the surge tank position, Renew. Energy 148 (2020) 478–491, http://dx.doi.org/10.1016/j.renene.2019.10.054.

[18] C. Liu, J. Zhou, X. Lai, T. Zhang, Optimization and mechanism of the wicket gate closing law for high-head pumped storage power stations, IEEE Access 9 (2021) 11734–11749, http://dx.doi.org/10.1109/ACCESS.2021.3049914.

[19] X. Mao, D. Chen, Y. Wang, G. Mao, Y. Zheng, Investigation on optimization of self-adaptive closure law for load rejection to a reversible pump turbine based on CFD, J. Clean. Prod. 283 (2021) 124739, http://dx.doi.org/10.1016/j.jclepro.2020.124739.

[20] B.-S. Kang, G.-J. Park, J.S. Arora, A review of optimization of structures subjected to transient loads, Struct. Multidiscip. Optim. 31 (2) (2006) 81–95, http://dx.doi.org/10.1007/s00158-005-0575-4.

[21] A. Sobester, A. Forrester, A. Keane, Engineering Design Via Surrogate Modelling: A Practical Guide, John Wiley & Sons, 2008.

[22] W.-L. Loh, On Latin hypercube sampling, Ann. Statist. 24 (5) (1996) 2058–2080.

[23] OpenCFD, OpenFOAM - The Open Source CFD Toolbox - User's Guide, Version v2012, OpenCFD Ltd., 2020.

[24] J. Fahlbeck, H. Nilsson, S. Salehi, A head loss pressure boundary condition for hydraulic systems, OpenFOAM J. 2 (2022) 1–12, http://dx.doi.org/10.51560/ofj.v2.69.

[25] M. Joseph, J. Fahlbeck, M. Zangeneh, H. Nilsson, Optimized initial down-scaled model design of SD-CRPT D2.1, public v1.0, EC, 2020, https://alpheus-h2020.eu/ Available online: https://alpheus-h2020.eu/wp-content/uploads/2020/06/ALPHEUS_Deliverable_2.1_SD-CRPT_V1.0.pdf accessed on 17 February 2023.

[26] J. Fahlbeck, H. Nilsson, S. Salehi, Evaluation of startup time for a model contra-rotating pump-turbine in pump-mode, IOP Conf. Ser.: Earth Environ. Sci. 1079 (2022) 012034, http://dx.doi.org/10.1088/1755-1315/1079/1/012034.

[27] D. Whitley, A genetic algorithm tutorial, Stat. Comput. 4 (1994) 65–85, http://dx.doi.org/10.1007/BF00175354.

[28] K. Deb, Multi-objective optimisation using evolutionary algorithms: an introduction, in: Multi-Objective Evolutionary Optimisation for Product Design and Manufacturing, Springer, 2011, pp. 3–34.

[29] F.N. Fritsch, R.E. Carlson, Monotone piecewise cubic interpolation, SIAM J. Numer. Anal. 17 (2) (1980) 238–246, http://dx.doi.org/10.1137/0717021.

[30] R. Tao, X. Zhou, B. Xu, Z. Wang, Numerical investigation of the flow regime and cavitation in the vanes of reversible pump-turbine during pump mode's starting up, Renew. Energy 141 (2019) 9–19, http://dx.doi.org/10.1016/j.renene.2019.03.108.

[31] A. Savitzky, M.J.E. Golay, Smoothing and differentiation of data by simplified least squares procedures, Anal. Chem. 36 (8) (1964) 1627–1639, http://dx.doi.org/10.1021/ac60214a047.

[32] C.E. Rasmussen, C.K. Williams, Gaussian Processes for Machine Learning, MIT press Cambridge, MA, 2006.

[33] S. Rogers, M. Girolami, A First Course in Machine Learning, Chapman and Hall/CRC, 2016.

[34] B. Williams, S. Cremaschi, Selection of surrogate modeling techniques for surface approximation and surrogate-based optimization, Chem. Eng. Res. Des. 170 (2021) 76–89, http://dx.doi.org/10.1016/j.cherd.2021.03.028.

[35] C.E. Rasmussen, Gaussian processes in machine learning, in: O. Bousquet, U. von Luxburg, G. Rätsch (Eds.), Advanced Lectures on Machine Learning: ML Summer Schools 2003, Canberra, Australia, February 2 - 14, 2003, Tübingen, Germany, August 4 - 16, 2003, Revised Lectures, in: Lecture Notes in Computer Science, Springer, Berlin, Heidelberg, 2004, pp. 63–71, http://dx.doi.org/10.1007/978-3-540-28650-9_4.

[36] F. Jäkel, B. Schölkopf, F.A. Wichmann, A tutorial on kernel methods for categorization, J. Math. Psych. 51 (6) (2007) 343–358, http://dx.doi.org/10.1016/j.jmp.2007.06.002.

[37] E. Schulz, M. Speekenbrink, A. Krause, A tutorial on Gaussian process regression: Modelling, exploring, and exploiting functions, J. Math. Psych. 85 (2018) 1–16, http://dx.doi.org/10.1016/j.jmp.2018.03.001.

[38] B. Matérn, Spatial variation, in: Meddelanden Från Statens Skogsforskningsinstitut, Vol. 49, 1960, p. 144, (5).

[39] W. Gao, M. Karbasi, M. Hasanipanah, X. Zhang, J. Guo, Developing GPR model for forecasting the rock fragmentation in surface mines, Eng. Comput. 34 (2) (2018) 339–345, http://dx.doi.org/10.1007/s00366-017-0544-8.

[40] D.R. Jones, M. Schonlau, W.J. Welch, Efficient global optimization of expensive black-box functions, J. Global Optim. 13 (4) (1998) 455–492, http://dx.doi.org/10.1023/A:1008306431147.

[41] H.G. Weller, G. Tabor, H. Jasak, C. Fureby, A tensorial approach to computational continuum mechanics using object-oriented techniques, Comput. Phys. 12 (6) (1998) 620, http://dx.doi.org/10.1063/1.168744.

[42] H.K. Versteeg, W. Malalasekera, An Introduction To Computational Fluid Dynamics: The Finite Volume Method, Pearson education, 2007.

[43] F. Menter, Y. Egorov, A scale adaptive simulation model using two-equation models, in: 43rd AIAA Aerospace Sciences Meeting and Exhibit, 2005, p. 1095, http://dx.doi.org/10.2514/6.2005-1095.

[44] F.R. Menter, Y. Egorov, The scale-adaptive simulation method for unsteady turbulent flow predictions. part 1: Theory and model description, Flow Turbul. Combust. 85 (1) (2010) 113–138, http://dx.doi.org/10.1007/s10494-010-9264-5.

[45] C. Trivedi, Investigations of compressible turbulent flow in a high-head francis turbine, J. Fluids Eng. 140 (1) (2017) http://dx.doi.org/10.1115/1.4037500.

[46] J. Unterluggauer, V. Sulzgruber, E. Doujak, C. Bauer, Experimental and numerical study of a prototype Francis turbine startup, Renew. Energy 157 (2020) 1212–1221, http://dx.doi.org/10.1016/j.renene.2020.04.156.

[47] S. Salehi, H. Nilsson, E. Lillberg, N. Edh, An in-depth numerical analysis of transient flow field in a Francis turbine during shutdown, Renew. Energy 179 (2021) 2322–2347, http://dx.doi.org/10.1016/j.renene.2021.07.107.

[48] J.-W. Suh, H.-M. Yang, J.-H. Kim, W.-G. Joo, J. Park, Y.-S. Choi, Unstable S-shaped characteristics of a pump-turbine unit in a lab-scale model, Renew. Energy (2021) http://dx.doi.org/10.1016/j.renene.2021.03.013.

[49] S. Salehi, H. Nilsson, Flow-induced pulsations in Francis turbines during startup - A consequence of an intermittent energy system, Renew. Energy 188 (2022) 1166–1183, http://dx.doi.org/10.1016/j.renene.2022.01.111.

[50] S. Salehi, H. Nilsson, Effects of uncertainties in positioning of PIV plane on validation of CFD results of a high-head Francis turbine model, Renew. Energy (2022) http://dx.doi.org/10.1016/j.renene.2022.04.018.

[51] P.E. Farrell, J.R. Maddison, Conservative interpolation between volume meshes by local Galerkin projection, Comput. Methods Appl. Mech. Engrg. 200 (1) (2011) 89–100, http://dx.doi.org/10.1016/j.cma.2010.07.015.

[52] H.J. Aguerre, S. Márquez Damián, J.M. Gimenez, N.M. Nigro, Conservative handling of arbitrary non-conformal interfaces using an efficient supermesh, J. Comput. Phys. 335 (2017) 21–49, http://dx.doi.org/10.1016/j.jcp.2017.01.018.

[53] H. Jasak, Error Analysis and Estimation for the Finite Volume Method with Applications To Fluid Flows, Imperial College London (University of London), 1996.

[54] J. Tu, G.-H. Yeoh, C. Liu, Chapter 6 - CFD solution analysis: Essentials, in: Computational Fluid Dynamics (Third Edition), Butterworth-Heinemann, 2018, pp. 211–253, http://dx.doi.org/10.1016/B978-0-08-101127-0.00006-4.

[55] H. Weller, Controlling the computational modes of the arbitrarily structured c grid, Mon. Weather Rev. 140 (10) (2012) 3220–3234, http://dx.doi.org/10.1175/MWR-D-11-00221.1.

[56] E. Robertson, V. Choudhury, S. Bhushan, D.K. Walters, Validation of OpenFOAM numerical methods and turbulence models for incompressible bluff body flows, Comput. & Fluids 123 (2015) 122–145, http://dx.doi.org/10.1016/j.compfluid.2015.09.010.

[57] R.I. Issa, Solution of the implicitly discretised fluid flow equations by operator-splitting, J. Comput. Phys. 62 (1) (1986) 40–65, http://dx.doi.org/10.1016/0021-9991(86)90099-9.

[58] S.V. Patankar, D.B. Spalding, A calculation procedure for heat, mass and momentum transfer in three-dimensional parabolic flows, Int. J. Heat Mass Transfer 15 (10) (1972) 1787–1806, http://dx.doi.org/10.1016/0017-9310(72)90054-3.

[59] F.M. White, Fluid Mechanics., eighth ed., McGraw-Hill, 2016.

[60] I.B. Celik, U. Ghia, P.J. Roache, C.J. Freitas, Procedure for estimation and reporting of uncertainty due to discretization in CFD applications, J. Fluids Eng.-Trans. ASME 130 (7) (2008) http://dx.doi.org/10.1115/1.2960953.

[61] A. Meana-Fernández, J.M. Fernández Oro, K.M. Argüelles Díaz, M. Galdo-Vega, S. Velarde-Suárez, Application of Richardson extrapolation method to the CFD simulation of vertical-axis wind turbines and analysis of the flow field, Eng. Appl. Comput. Fluid Mech. 13 (1) (2019) 359–376, http://dx.doi.org/10.1080/19942060.2019.1596160.

[62] J. Jeong, F. Hussain, On the identification of a vortex, J. Fluid Mech. 285 (1995) 69–94.